WILEY | Hindawi

Research Article

Evaluation and Performance Testing of Eccentric Rolling Isolation System

Cho-Yen Yang [iD],[1] **Dan Chiao** [iD],[2] **Yong-An Lai** [iD],[3] **Chia-Ming Chang** [iD],[4] **and Lap-Loi Chung** [iD][1]

[1]*National Center for Research on Earthquake Engineering, Taipei 106219, Taiwan*
[2]*Evergreen Consulting Engineering, Inc., Taipei 106213, Taiwan*
[3]*Department of Civil Engineering, National Central University, Taoyuan 320317, Taiwan*
[4]*Department of Civil Engineering, National Taiwan University, Taipei 106319, Taiwan*

Correspondence should be addressed to Cho-Yen Yang; cyyang@ncree.narl.org.tw

Seismic isolation has become a widely accepted method for the protection of structures and nonstructural components. However, this control strategy is unfavorable against near-fault earthquakes, particularly those featuring velocity-pulse effects. Excessive isolation displacements and accelerations can occur during such earthquakes, resulting in amplified responses of the superstructure. To resolve this problem, this study develops a prototype of the eccentric rolling isolation system consisting of one platform eccentrically pin-connected to four circular rollers. The eccentric pin connection yields a nonlinear restoring force of the proposed system and results in displacement-dependent resonances, and the inherent mechanical friction also yields an energy dissipation capability of the system. As the magnitude of ground excitation increases, the prototype system generates a lower resonant frequency away from the dominant frequencies of earthquakes. This behavior is experimentally investigated and verified for mechanical behavior and seismic performance. In the experiment, sinusoidal, far-field, and near-fault ground motions are considered in shaking table testing. Some parameters, such as the eccentricity, roller size, and inertial force, are also experimentally investigated. As found in the experimental result, the feasibility of the prototype system is successfully verified. Meanwhile, the comparable simulation results further validate the mathematical model of the prototype system. Consequently, the eccentric rolling isolation system has demonstrated isolation effectiveness against far-field ground motions and has good potential to perform better than a linear system under near-fault ground motions.

1. Introduction

Seismic isolation technologies have been studied and proven to be an effective way to mitigate ground acceleration transmission to a superstructure [1]. The function of isolation systems is to shift the fundamental period of a structure from a shorter to a longer period by placing horizontally flexible isolation bearings between the superstructure and the base. By introducing the isolation system, the fundamental period of the structure can be shifted away from the dominant period of the ground motion, usually by approximately one second [2]. Such isolation technologies are implemented in the industry for seismic protection of buildings [3–8]. The same technologies can be employed to protect essential components and equipment against earthquakes [9, 10].

The issue of near-fault ground motion has led to further investigation of the seismic performance of long-period structures excited by ground motions that also possess long-period (or low-frequency) content. This kind of ground motion is usually observed at sites near seismic faults, and it creates an important near-fault issue for seismic isolation [11–13]. An isolation system is usually designed to have an isolation period of 2–5 s, which is quite effective at reducing the structural response under most earthquakes. However, the isolation period of 2–5 s coincides with the dominant periods of near-fault ground motions. Thus, the response of the isolated structure can be remarkably amplified.

The effectiveness of isolation systems is negatively impacted, and moat wall pounding may occur due to the excessive isolation displacement under near-fault ground motions [14]. Even if the isolation system is designed to accommodate the isolation displacement under the maximum considered earthquake [15], which is a rare event, the isolation displacement would still probably exceed the design displacement under near-fault ground motion with an intensity lower than the design earthquake.

Adding damping with isolators is an option to reduce excessive responses during near-fault earthquakes. For example, Jangid [16, 17] investigated the seismic performance of both lead rubber bearings and friction pendulum bearings under near-fault motions. As found, both hysteretic and friction-damping effects can reduce the isolation displacement without significantly increasing the acceleration of the superstructure, which is also effective in improving the structural performance against near-fault ground motions. A sufficiently large damping level can be essential for near-fault ground motions; however, this large damping becomes a negative effect in far-field earthquakes, e.g., resulting in higher story drifts [18, 19]. Recently, an interesting implementation of rate-independent linear damping (RILD), for long-period structures subjected to near-fault ground motions, was also investigated [20–23]. The key feature of the RILD relative to the conventional linear viscous damper is that the RILD generates a higher damping force in the frequency region which is lower than the fundamental frequency of the system to suppress the displacement. By using this key feature of RILD, the implementation of RILD to prevent excessive displacement of the isolation system under near-fault ground motions was also verified [24–26]. However, designing an isolated structure under both far-field and near-fault ground motions is challenging.

Alternatively, isolation systems with variable stiffness are another strategy to enhance the seismic performance of structures. The variable stiffness can provide nonlinear restoring forces and increase the effectiveness of isolation systems against near-fault earthquakes [27–29]. These isolation systems with variable stiffness may possess a broader frequency bandwidth to be effective under both far-field and near-fault ground motions. This feature can be realized in sliding isolators in which the sliding surface is formed by variable curvatures, e.g., polynomial shapes [30–32]. Some researchers employed quasizero stiffness in isolation systems to generate almost zero stiffness around the equilibrium, resulting in extra low resonance initially [33–36]. In other words, the frequency content of external excitations is hard to lower than that extra low isolation frequency, which ensures the isolation effectiveness.

In addition to the conventional roller isolation bearings, the nonlinear restoring force can be generated not only from a nonlinear rolling surface but also from circular rollers with eccentric axles (hereafter denoted eccentric pin connections). Thus, the eccentric rolling isolation system (ERIS), which is a rolling-type isolation system, was proposed by Chung et al. [37], and its effectiveness with friction damping was further studied by Yang et al. [38]. "Eccentricity" is the concept underlying ERIS, in which the isolation object or superstructure is pin-connected to the circular isolator (roller) eccentrically. Due to the eccentric pin connection, the restoring force performs nonlinearly and depends on the rolling angle. The eccentricity and radius of the circular isolator (roller) are the two most basic and important design parameters that govern the nonlinearity of the relationship between the restoring force and the rolling angle. The feasibility of ERIS has been numerically verified in previous studies [37, 38]. The simulation results also showed that ERIS attenuates amplification under resonance and can be more effective than a linear system under near-fault ground motions. However, the research was conducted based on theoretical and numerical analyses, and experimental verification is needed to understand applicability in practical use.

The objective of this research is to conduct shaking table testing for a prototype eccentric rolling isolation system and verify the analytical findings in the previous research. The equation of motion of ERIS is briefly reviewed and modified due to the consideration of the inertial effect of the roller. Then, parametric studies are carried out to demonstrate the effects on the overall dynamics of this system which are governed by several important parameters. A prototype ERIS is then fabricated in-house, and various dynamic loadings, including sinusoidal, far-field, and near-fault ground motions, are used as the inputs to this prototype ERIS for performance evaluation. As found in the experimental results, the friction coefficient of the system is first identified. Once the friction coefficient is obtained, the analytical model is verified by comparing the experimental and simulation results. Based on the verified analytical model, the prototype ERIS could be numerically studied for additional cases that exceed the capacity limitation of the shaking table. Finally, the seismic performances of the proposed prototype of ERIS are investigated in detail based on both the experimental and simulation results.

2. Mathematical Model and Numerical Simulation

The derivation of the equation of motion and the numerical simulation procedure of ERIS is briefly introduced here. The prototype ERIS is assumed to be implemented in equipment isolation, which means that the superstructure is simplified as a rigid body (Figure 1). The simulation program was coded in MATLAB software [39], and the function "ode45" based on the Runge–Kutta method is adopted to solve the nonlinear equation of motion.

2.1. Equation of Motion. The schematic mechanism of ERIS is visually similar to a conventional slide or a car with four wheels. However, its platform is eccentrically pin-connected at a distance αR from the center of the circular roller (Figure 2). The shift distance αR is defined by the eccentricity α times the radius of the roller R. The force of the lumped mass of the rigid-body superstructure and platform, denoted by m_i, can be applied at the eccentric pin. In past research, the total mass of the rollers was neglected (i.e., $m_r = 0$) due to
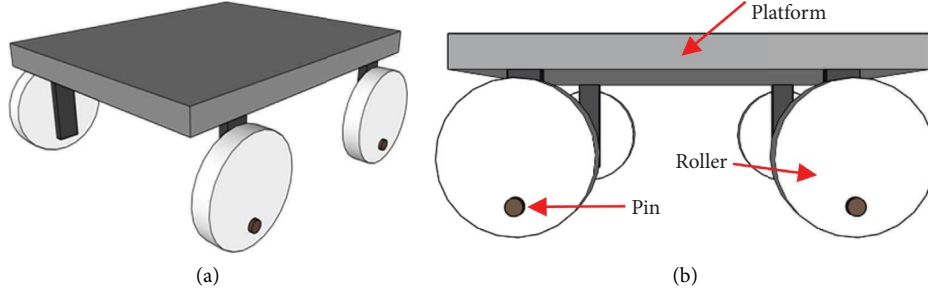
FIGURE 1: Schematic diagram of ERIS. (a) 3D schematic diagram of ERIS. (b) Side view of ERIS.

I: Platform   III: Rigid link   V: Socket set screw
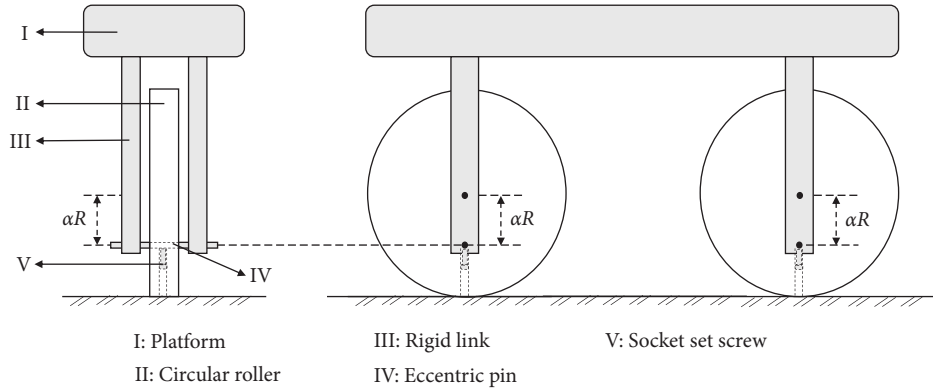
II: Circular roller   IV: Eccentric pin

FIGURE 2: Detailed mechanical concept of ERIS.

the assumption of the mass of the superstructure being much larger than the mass of the roller (i.e., $m_i \gg m_r$). However, if the application of ERIS is for equipment isolation, the above assumption is not valid. Therefore, the mass of the roller is taken into consideration to investigate the inertial effect of the roller.

From Figure 3, it is clear that the position of the superstructure ($\mathbf{X}_i$) and roller ($\mathbf{X}_r$) can be represented by the rolling angle θ which is the only degree of freedom in the system. The two displacement vectors are given in the following equation:

$$\begin{cases} \mathbf{X}_i = \left[x_g + (R\theta - \alpha R \sin \theta) \right] \vec{i} + [R - \alpha R \cos \theta] \vec{j}, \\ \mathbf{X}_r = \left[x_g + R\theta \right] \vec{i} + [R] \vec{j}, \end{cases} \quad (1)$$

where vectors $\vec{i}$ and $\vec{j}$ denote the unit vectors in the horizontal and vertical directions, respectively, and x_g is the ground displacement.

The velocity and acceleration vectors can be obtained by taking the time derivative of the displacement vectors in equation (1), once to obtain equation (2) and twice to obtain equation (3):

$$\begin{cases} \mathbf{V}_i = \left[\dot{x}_g + (R - \alpha R \cos \theta)\dot{\theta} \right] \vec{i} + [\alpha R \sin \theta \cdot \dot{\theta}] \vec{j}, \\ \mathbf{V}_r = \left[\dot{x}_g + R \cdot \dot{\theta} \right] \vec{i}, \end{cases} \quad (2)$$

$$\begin{cases} \mathbf{A}_i = \left[\ddot{x}_g + (R - \alpha R \cos \theta)\ddot{\theta} + \alpha R \sin \theta \cdot \dot{\theta}^2 \right] \vec{i} + \left[\alpha R \sin \theta \cdot \ddot{\theta} + \alpha R \cos \theta \cdot \dot{\theta}^2 \right] \vec{j}, \\ \mathbf{A}_r = \left[\ddot{x}_g + R \cdot \ddot{\theta} \right] \vec{i}. \end{cases} \quad (3)$$

To derive the equation of motion, the energy method is employed by introducing Lagrange's equation [40] as follows:

$$\frac{d}{dt} \left(\frac{\partial L}{\dot{\theta}} \right) - \frac{\partial L}{\theta} = Q^N, \quad (4)$$

where the Lagrangian, L, represents the difference between the kinetic and potential energy of the system (equation (5)) and Q^N is a nonconservative force corresponding to the degree of freedom.
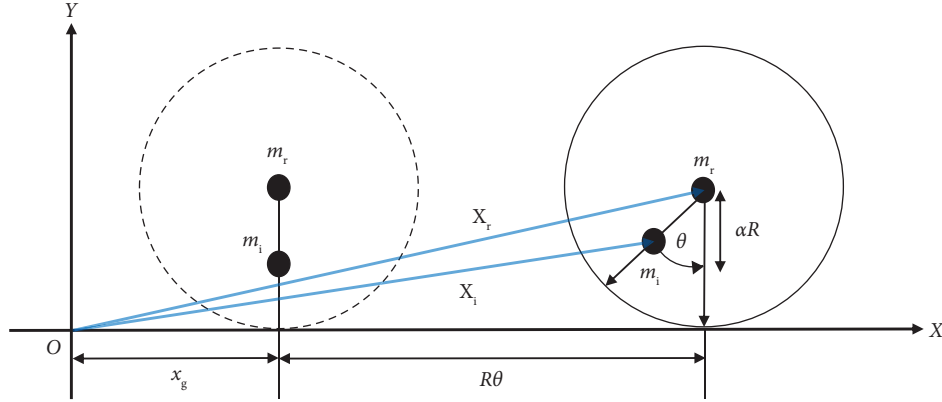
$$L = T - U. \quad (5)$$

FIGURE 3: Coordinate definition of ERIS for the mathematical model.

The kinetic and potential energy can be calculated from equations (6) and (7) as

$$
\begin{aligned}
T &= \frac{1}{2}m_i V_i^{\,2} + \frac{1}{2}m_r V_r^{\,2} + \frac{1}{2}I_r\dot{\theta}^2 \\
&= \frac{1}{2}m_i\left[\dot{x}_g^2 + 2R\dot{x}_g\dot{\theta} - 2\alpha R(\cos\theta)\dot{x}_g\dot{\theta} + R^2\dot{\theta}^2 - 2\alpha R^2(\cos\theta)\dot{\theta}^2 + \alpha^2 R^2\dot{\theta}^2\right] \\
&\quad + \frac{1}{2}m_r\left(\dot{x}_g^2 + R^2\dot{\theta}^2 + 2R\dot{x}_g\dot{\theta}\right) + \frac{1}{4}m_r R^2\dot{\theta}^2,
\end{aligned}
\tag{6}
$$

$$
U = m_i g\alpha R(1 - \cos\theta),
\tag{7}
$$

where g is the acceleration due to gravity and I_r is the rotational inertia of the roller. In equations (6) and (7), it is noted that the kinetic energy of the roller is added to the system, but it does not affect the potential energy while the whole system is in motion. To be considered a reasonable isolation system, it must be capable of energy dissipation and the frictional damping of Coulomb's model is introduced in this paper. The nonconservative force M_{fr} can be determined from the normal force N times the friction coefficient μ_d and moment arm R as

$$
Q^N = -M_{\mathrm{fr}} = -\mu_d NR\,\mathrm{sgn}(\dot{\theta}).
\tag{8}
$$

It is notable that the friction model in equation (8) provides effective frictional damping in the system because of the complexity of the determination of the friction force in the mechanism, such as the pin and rolling friction. In this paper, the normal force due to the total weight of the superstructure and roller is adopted (i.e., $N = (m_i + m_r)g$), and the friction coefficient μ_d is further determined by the experimental results.

Once the kinetic energy, potential energy, and nonconservative force are determined, the equation of motion can be further obtained by substituting equations (6) to (8) into equation (4), and after reordering the derivation, the equation of motion then becomes

$$
\begin{aligned}
R^2\left[m_i\left(\alpha^2 - 2\alpha\cos\theta + 1\right) + \frac{3}{2}m_r\right]\ddot{\theta} + m_i g\alpha R\sin\theta + m_i\alpha R^2(\sin\theta)\dot{\theta}^2 + M_{\mathrm{fr}} \\
= R\left[m_i(\alpha\cos\theta - 1) - m_r\right]\ddot{x}_g.
\end{aligned}
\tag{9}
$$

The nonlinear equation of motion in equation (9) is used in the following numerical simulation, including the parametric study and resimulation to compare with the experimental results. As compared to the conventional linear isolation system, the isolation frequency is no longer fixed due to the nonlinearity of the system (equation (9)). To provide a more straightforward understanding of ERIS compared to the linear system, a small rolling angle is

considered and the high-order term is assumed to be negligible. The original equation of motion in equation (9) can be linearized as

$$R^2\left[m_i(\alpha-1)^2+\frac{3}{2}m_r\right]\ddot{\theta}+m_ig\alpha R\theta+M_{\text{fr}}=R\left[m_i(\alpha-1)-m_r\right]\ddot{x}_g. \qquad (10)$$

According to the linearized equation of motion in equation (10), the linearized frequency of ERIS f_0 can be determined from equation (11) as

$$f_0=\frac{1}{2\pi}\sqrt{\frac{\alpha g}{R\left[(\alpha-1)^2+(3/2)r_m\right]}}, \qquad (11)$$

where r_m is a mass ratio defined as m_r/m_i. The linearized frequency of ERIS is governed by three parameters: eccentricity, the radius of the roller, and the mass ratio. The frequency decreases with an increase in the radius and mass ratio but increases with an increase in eccentricity. When the mass of the roller is ignored, the result of equation (11) matches the result derived from previous research [37]. By introducing the mass of the roller, the implementation of ERIS becomes easier because a longer isolation period (lower frequency) can be obtained without using a larger radius R. Furthermore, equation (11) also implies that the isolation frequency may be underestimated if the mass of the roller is ignored when ERIS is implemented for equipment isolation. This underestimation of the isolation frequency also implies an underestimation of stiffness and may further result in an underestimation of isolation displacement.

2.2. Numerical Integration. To further investigate the dynamic behavior of ERIS under excitation, the nonlinear equation of motion is numerically solved by calling the function "ode45" in MATLAB, which uses the Runge–Kutta method. The state of the system includes the rolling angle, velocity, frictional moment, and excitation, which should be known at the current time step k. However, the frictional force at the current time step $M_{\text{fr}}[k]$ is unknown. To determine the friction force at the current time step, the first-order discrete-time difference equation of rolling velocity is introduced as

$$\dot{\theta}[k+1]=\dot{\theta}[k]+\Delta t\ddot{\theta}[k], \qquad (12)$$

where Δt is the sampling time interval. For a dynamical system with friction damping, the state of the system can be divided into two states: slip and stick. If the system is assumed to be in a stick state, the rolling velocity is zero (i.e., $\dot{\theta}[k+1]=0$). Setting equation (12) equal to zero and replacing the rolling acceleration by substituting the equation of motion into equation (12), the prediction of the frictional force $\tilde{M}_{\text{fr}}$ can be calculated as per equation (13):

$$\tilde{M}_{\text{fr}}=-m_iR\left\{(1-\alpha\cos\theta+r_m)\ddot{x}_g+\alpha R\sin\theta\cdot\dot{\theta}^2+g\alpha\sin\theta\right\}$$
$$+\frac{m_iR^2\left\{1+\alpha^2-2\alpha\cos\theta+(3/2)r_m\right\}\dot{\theta}}{\Delta t}. \qquad (13)$$

In equation (13), the time variable is neglected for simplicity. If Coulomb's model is introduced, the prediction of the friction force in equation (13) should not exceed the maximum friction force when the system is in the stick state. On the contrary, if the prediction of the friction force is greater than the maximum friction force, the stick assumption is invalid. Thus, the exact friction moment equals the maximum friction force. Consequently, the friction force at the current time step can be expressed as

$$M_{\text{fr}}[k]=\min\left(\left|\tilde{M}_{\text{fr}}[k]\right|,\mu_dNR\right)\text{sgn}\left(\tilde{M}_{\text{fr}}[k]\right), \qquad (14)$$

where $\text{sgn}(\cdot)$ presents the sign function. After the friction force of ERIS at the current time step is determined by equation (14), the full state of the system is known and then the ODE solver can be called to calculate the state in the next time step. The entire time history response of ERIS can be obtained by repeating this procedure.

2.3. Parametric Study. The mathematical model of ERIS and the simulation procedure are introduced in previous sections. The sensitivity of several design parameters is also briefly introduced, especially the sensitivity of the mass ratio, and a detailed discussion of the other parameters can be found in the literature [37, 38]. In the following two sections, a standard set of system parameters is set as follows: the mass of the superstructure m_i and roller m_r are set at 10 kg and 8 kg, respectively (i.e., $r_m=0.8$), and the radius R and eccentricity α are set at 7.5 cm and 0.3, respectively. For the two parameters of friction damping, the friction coefficient μ_d and normal force N are set to 0.02 and 176.58 N, respectively. From the derivation of the equation of motion in the previous section, it is clear that ERIS is a nonlinear system due to its eccentricity, which implies that the frequency of the system varies with displacement (rolling angle). To demonstrate the variation of the frequency of ERIS, undamped free vibration with the initial angle varying from 1° to 150° with an interval of one degree is conducted for various eccentricities, radii, and mass ratios.

2.3.1. Effect of Eccentricity. Figure 4(a) illustrates the sensitivity of eccentricity to the variation of frequency. For any specific eccentricity, the frequency of ERIS decreases with an increase in the initial angle, and it approaches the linearized frequency defined in equation (11) when the initial angle is small (i.e., $\theta_0 \approx 0$). Using an eccentricity of 0.3 as an example, the frequency varies from 0.767 Hz to 0.365 Hz when the initial angle increases from 1° to 150°. The greater the eccentricity, the larger the variation of the frequency. On the other hand, for any specific initial angle, the greater the eccentricity, the higher the frequency. Thus, for lower isolation frequencies (or longer periods), a large value should not be specified for the eccentricity in the practical applications of ERIS.

2.3.2. Effect of Radius. Similarly, the influence of the radius on the frequency is illustrated in Figure 4(b). The radius of the roller plays the same role as the curvature of the conventional friction pendulum bearing: the greater the radius, the lower the isolation frequency (or the longer the period). For the case of the radius being equal to 2.5 cm, the frequency varies from 1.328 Hz to 0.632 Hz with the considered range of the initial angle. However, for the case of a radius equal to 12.5 cm, the frequency varies from 0.594 Hz to 0.282 Hz with the same range of the initial angle. It is notable that an ERIS with a large radius also possesses a large isolation displacement when compared with a case with a small radius under the same initial angle.

2.3.3. Effect of Mass Ratio. The mass ratio similarly affects the frequency of the system: the greater the mass ratio, the lower the isolation frequency (or the longer the period) (Figure 4(c)). The variation of the frequency generally decreases with an increase in the mass ratio. To sum up, an engineer can select a larger radius or mass ratio or a smaller eccentricity to implement ERIS with a longer isolation period.

2.4. Seismic Performance. To better discuss and demonstrate the seismic performance of ERIS, three simple performance indices, the displacement, horizontal acceleration, and vertical acceleration ratios, are, respectively, defined as

$$r_d = \frac{\max|x_i(t)|}{\pi R}, \tag{15}$$

$$r_a = \frac{\max|\ddot{x}_{i,\text{abs}}(t)|}{\text{PGA}}, \tag{16a}$$

$$r_{a,v} = \frac{\max|\ddot{x}_{i,v}(t)|}{\text{PGA}}. \tag{16b}$$

Intuitively, ERIS can only be stable when the rolling angle θ is smaller than ±180 degrees (i.e., ±π). Thus, the horizontal displacement relative to the ground x_i is normalized by half of the perimeter πR. The displacement ratio must be smaller than one; otherwise, the system is unstable. The displacement x_i can be calculated by removing the

ground displacement term x_g from the horizontal component of $\mathbf{X}_i$ in equation (1) for numerical simulation (i.e., $x_i = R\theta - \alpha R \sin \theta$) or be directly measured by the displacement transducer during testing. In addition to isolation displacement, the effectiveness of the acceleration after isolation being normalized by the peak ground acceleration (PGA) is also a simple way to determine acceleration reduction. For an isolation system, the smaller the acceleration ratio, the higher its effectiveness. Similarly, the horizontal absolute acceleration after isolation $\ddot{x}_{i,\text{abs}}$ can be calculated by taking the horizontal component of $\mathbf{A}_i$ in equation (3) for numerical simulation or measured by an accelerometer during testing. Additionally, the vertical acceleration ratio $r_{a,v}$ is also introduced, which has a similar definition as horizontal acceleration ratio, but with the numerator replaced by the peak value of the vertical acceleration. The vertical acceleration $\ddot{x}_{i,v}$ could be obtained by measurement from a vertical accelerometer or calculated by taking the vertical component of $\mathbf{A}_i$ in equation (3) for numerical simulation.

3. Shaking Table Test and Resimulation

3.1. Test Setup. The prototype of the specimen is illustrated in Figure 5. To avoid slip between the circular roller and the ground while the system is in motion, four spur gears, i.e., rollers rolling on two racks, are adopted. The whole specimen is installed on a uniaxial shaking table. According to the standard production of spurs provided by the industry, existing spur gears of module 1.5 with 70 and 100 teeth are adopted (i.e., SSA-1.5-70 and SSA-1.5-100) [41]. The radii of the two selected spur gears are 5.25 cm and 7.5 cm. In this paper, the radius of the spur gear with a radius of 5.25 cm is denoted as 5 cm for simplicity. For each type of roller, two through-holes corresponding to eccentricities 0.2 and 0.3 are drilled shown in Figure 6. The corresponding rack is determined by the module of the spur gear (i.e., SRF-1.5-1000) [41].

Four specimens are designed to investigate the effect of three key parameters, the radius, eccentricity, and mass ratio, on the dynamic behavior of ERIS subject to ground excitations. Detailed specifications are tabulated in Table 1. Taking specimens SP1 and SP2 as an example, all parameters are the same except for the eccentricity; thus, the behavior of the system under different eccentricities can be compared and studied. Similarly, the effect of the mass ratio and radius can be investigated by comparing the experimental results between SP2 and SP3, and SP3 and SP4, respectively. It should be noted that for SP3 and SP4, the mass ratio is similar but not identical; the reason for this is that the mass of the superstructure was only adjusted using the small steel mass blocks already available in the laboratory. The linearized frequencies, which are the highest frequencies of the four specimens in motion, are also provided in Table 1.

The instrument layout and specimen setup for the four specimens are shown in Figures 7(a) and 7(b). To measure the absolute acceleration response after isolation, three accelerometers are installed on the platform, two of them for the horizontal and one for the vertical direction. The two
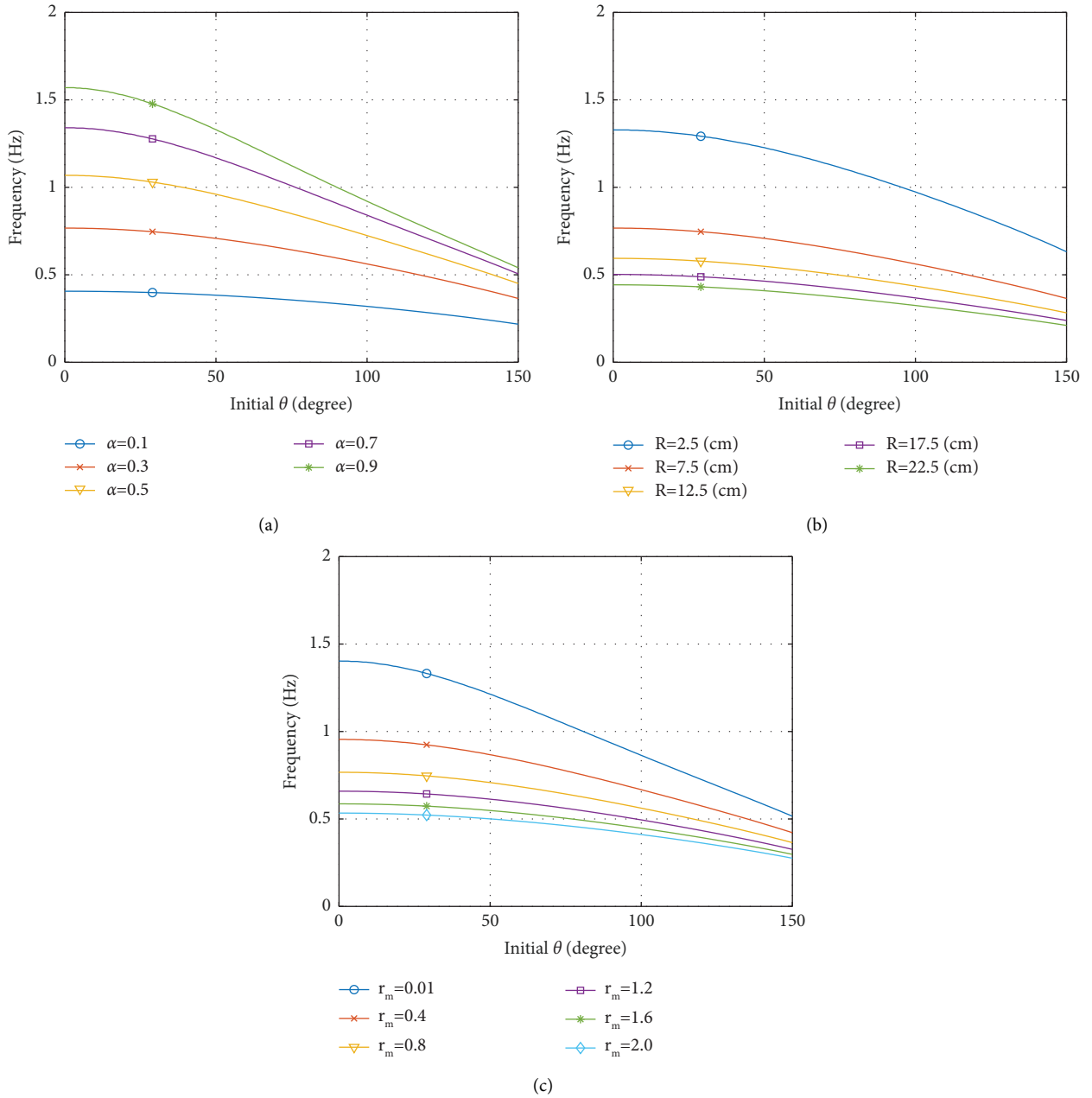
FIGURE 4: Sensitivity of isolation frequency due to (a) eccentricity; (b) radius of circular roller; (c) mass ratio.
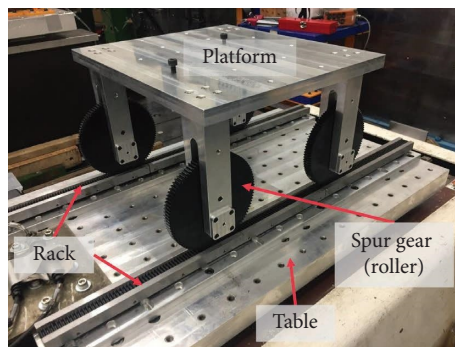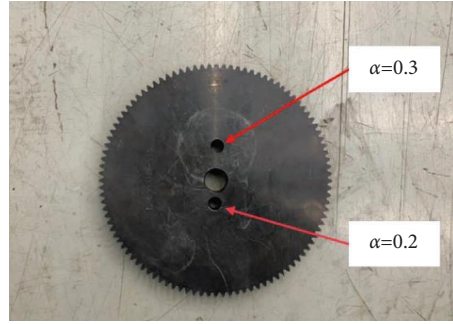

FIGURE 5: Prototype of specimen.

FIGURE 6: Roller with two eccentricities.

TABLE 1: Specification of specimens.

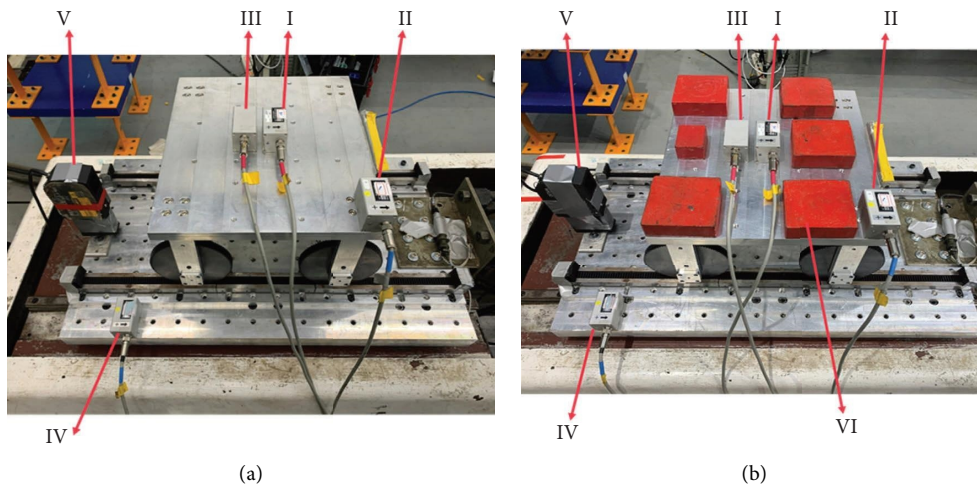| Specimen	R (cm)	α	m_r(kg)	m_i (kg)	r_m	f_0 (HZ)	$\overline{\mu}_d$
SP1	7.5	0.2	8.01	11.55	0.693	0.628	0.018
SP2	7.5	0.3	8.01	11.55	0.693	0.806	0.020
SP3	7.5	0.3	8.01	24.15	0.332	1.003	0.022
SP4	5	0.3	3.77	11.55	0.326	1.234	0.036

(a)

(b)

FIGURE 7: Test setup of specimens: (a) SP1, SP2, and SP4; (b) SP3 (I–IV: accelerometers; V: laser displacement transducer; VI: mass block).

horizontal accelerometers are installed at the center and the corner of the platform, with the latter considered a "dummy" and used to further check whether unexpected torsion occurred. The vertical acceleration, which is a trade-off, could be observed in a similar way as in applications using friction pendulum bearings or other bearings that use geometry to obtain a long isolation period. To make sure that the vertical acceleration is within an acceptable range when ERIS is tested, a vertical accelerometer is also installed at the center of the platform. In addition, an accelerometer is mounted on the shaking table to capture the ground acceleration during testing.

Isolation displacement, which reflects the cost of space, is an important index in practical applications. Engineers and researchers always try to maximize the effectiveness of acceleration and minimize isolation displacement. Thus, a laser displacement transducer placed parallel to the shaking table is used to measure the horizontal displacement

response of ERIS relative to the ground. To adjust the mass ratio in this case, additional steel mass blocks painted in red are attached to the platform for SP3, but the instrument layout remains the same as for the other three specimens, shown in Figure 7(b). The weight of the accelerometers on the platform is considered in the total weight of the superstructure m_i listed in Table 1. The uniaxial shaking table at the National Center for Research on Earthquake Engineering (NCREE) is used for this research. The size of the table is 80 cm × 50 cm, and the maximum force and stroke of the actuator are 15 kN and ±75 mm, respectively.

3.2. Test Program. To experimentally verify the seismic performance of ERIS, the four specimens are subjected to sinusoidal and seismic excitations. For the sinusoidal excitation, three frequencies, $0.5f_0$, f_0, and $2f_0$, are selected to investigate the response of the system subjected to

low-frequency, resonant frequency, and high-frequency cases. The linearized frequency f_0 corresponding to each specimen is adopted while the system is subjected to sinusoidal excitation. Three PGD amplitudes with twenty-three cycles (i.e., per amplitude) are implemented for a specific excitation frequency to explore the effect on ERIS further. To mitigate the transient response of the system, a linear increment for the first three cycles is also adopted. The test program for the sinusoidal excitation is tabulated in detail in Table 2. The shaking table is actuated by displacement control; thus, the input ground motions are converted to displacement commands, and all the amplitudes of the excitations are classified and denoted by PGD for convenience. Moreover, due to the stroke limitation of the actuator, ±75 mm, the maximum value of the PGD is set equal to 75 mm.

The seismic performance of ERIS subjected to earthquake loads is also evaluated. Two earthquake records of Imperial Valley-06 and Chi-Chi (TCU102, EW) are considered and detailed in Table 3. From the seismological perspective, the above two ground motions can be categorized as far-field and near-fault ground motions [42]. The original ground accelerations are illustrated in Figures 8(a) and 8(b), and the corresponding power spectral density diagrams with PGAs normalized to 1.0 g are also illustrated in Figure 8(c). Additionally, the two ground motions are filtered using a high-pass filter with 0.4 Hz to meet the stroke limitation of the actuator without removing too many long-period components and the acceleration response spectra with PGAs normalized to 1.0 g after filtering are shown in Figure 8(d). For each ground motion, three amplitudes are adopted for the shaking table tests in Table 4.

3.3. Experimental Results and Verification of the Mathematical Model.

In an experimental study, the measurement of a sensor, especially of an accelerometer, may contain high-frequency noise induced by the mechanism of the shaking table or other electronic devices such as the data logger or controller. Thus, all measurement data of the accelerometers are filtered using a low-pass filter at 10 Hz. Moreover, by comparing the two measurements of acceleration from the horizontal accelerometers I and II, they are quite close, and thus, no unexpected increase of friction or torsion occurs on this prototype. The mathematical model derived in the previous section is verified by comparing the resimulation results with the experimental results. Before resimulation, the friction coefficient of each specimen is determined by tuning and minimizing an objective function defined as the error of both the acceleration and displacement between the simulation and experimental result with a 50% weighting of each. The objective function J is defined as

$$\min_{\mu_d \in [0,1]} J(\mu_d) = 0.5 J_d + 0.5 J_a, \quad (17)$$

where J_a and J_d are two subobjective functions for acceleration and displacement, respectively, and are defined as

TABLE 2: Test items for sinusoidal excitation.

Excitation frequency	SP1	SP2	SP3	SP4
	PGD (cm)			
0.5 f_0	7.5	7.5	7.5	7.5
	7.0	7.0	7.0	7.0
	6.5	6.5	6.5	6.5
f_0	4.0	4.0	4.0	4.0
	3.0	3.0	3.0	3.0
	2.0	2.0	2.0	2.0
2 f_0	6.0	6.0	4.0	4.0
	4.0	4.0	3.0	3.0
	2.0	2.0	2.0	2.0

$$J_a = \frac{(1/n)\sum_{k=1}^{n}\left|a_e[k] - a_s[k]\right|}{\max\left(\left|a_e[k]\right|\right)}, \quad (18)$$

$$J_d = \frac{(1/n)\sum_{k=1}^{n}\left|d_e[k] - d_s[k]\right|}{\max\left(\left|d_e[k]\right|\right)}. \quad (19)$$

In equation (18), the total error of the horizontal absolute acceleration between the experimental result a_e and simulation result a_s for a specific test item was normalized by the total number of time steps n and the peak value of the acceleration a_e, determined from the experiment. The same concept is used to define the subobjective in the displacement in equation (19). For each test item, an optimal friction coefficient μ_d^* minimizing the objective function J can be obtained. For a specific specimen, the effective friction coefficient $\bar{\mu}_d$ in resimulation can be further determined by taking the average of μ_d^* corresponding to each test item (i.e., $\bar{\mu}_d = \sum_{\text{item}}\mu_d^*/N_{\text{item}}$). The resultant friction coefficients of the four specimens are listed in the last column of Table 1. For SP1, SP2, and SP3, the friction coefficient is roughly 2%; however, it increases to 3.6% for SP4. SP1, SP2, and SP3 share the same set of circular rollers (four spur gears with $R = 7.5$ cm). The circular rollers are replaced by four spur gears with $R = 5$ cm in SP4. This mechanical change is supposed to be the cause of its larger friction coefficient.

3.3.1. Free Vibration.

Before testing ERIS under seismic excitation, free vibration testing is first conducted to check whether the specimen would roll smoothly or not. The specimens are manually pulled to a position and then released to vibrate freely until rest. Figure 9 depicts the hysteresis comparison between the experimental and resimulation results for the four specimens with horizontal initial displacement equal to 16.71 cm, 16.37 cm, 17.45 cm, and 12.48 cm, respectively (sorted by ascending specimen name). The maximum shear forces from the experimental results sorted by ascending specimen name are 12.83 N, 17.46 N, 48.52 N, and 25.44 N, respectively. On the other hand, the maximum shear forces from the resimulations are 12.51 N, 17.55 N, 49.04 N, and 24.60 N, respectively. The simulation errors are 2.49%, 0.52%, 1.07%, and 3.28%, respectively. A comparison of the hysteresis for the four specimens in Figure 9 also shows that the simulation result approximates the experimental result closely. Thus, the

TABLE 3: Seismic records.

Type	Earthquake (year)	Station	Direction	PGA (g) PGD (cm)
Far-field	Imperial Valley-06 (1979)	Coachella Canal #4	135°	0.128 3.26
Near-fault	Chi-Chi (1999)	TCU102	EW	0.304 8.09

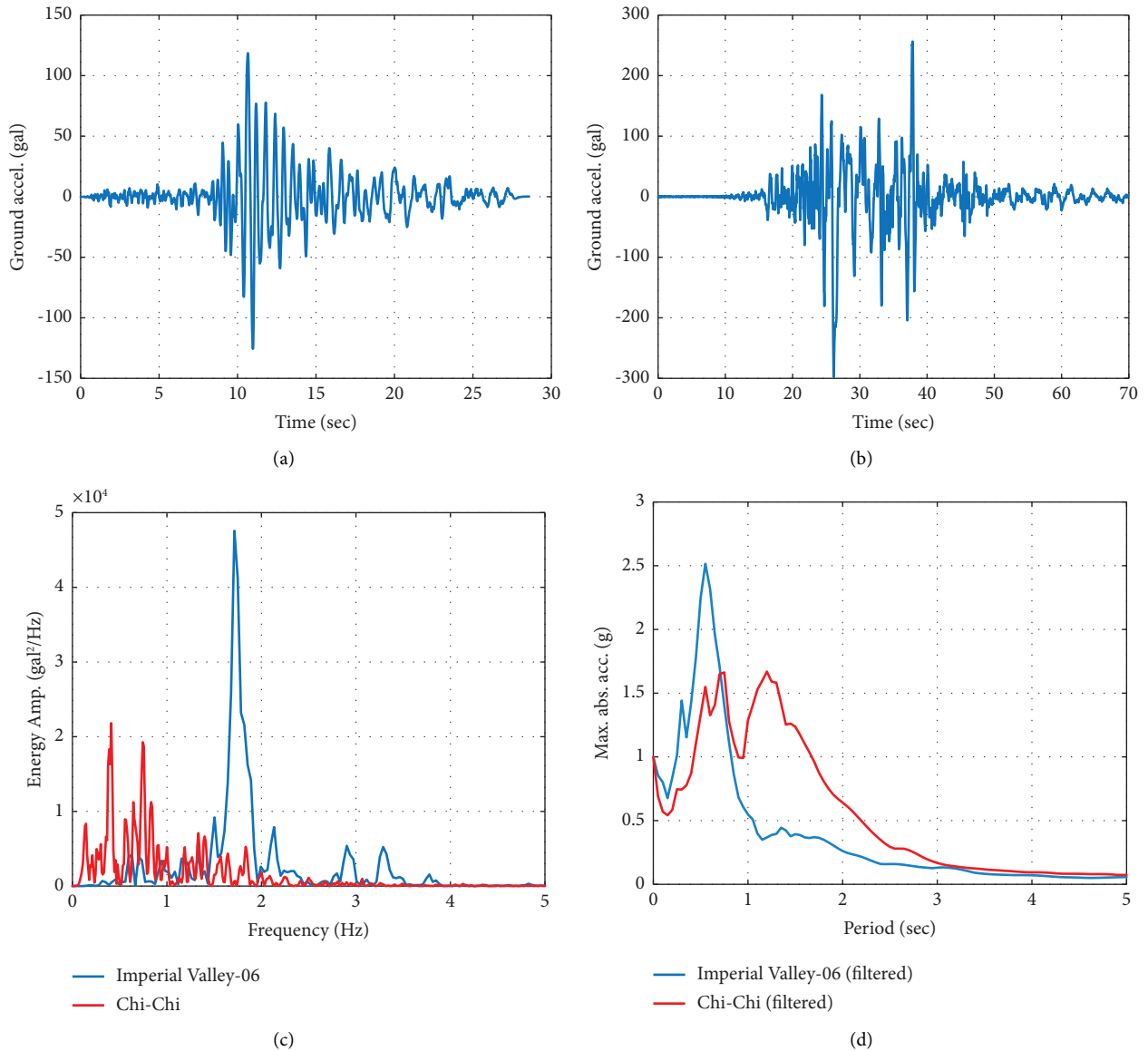*Note.* Estimated PGDs were obtained with baseline correction.

(a)

(b)

(c)

(d)

FIGURE 8: Ground excitations: (a) Imperial Valley-06, (b) Chi-Chi, (c) power spectral densities, and (d) acceleration response spectra.

behavior of ERIS can be accurately represented by numerical simulation using the mathematical model derived in the previous section.

3.3.2. Sinusoidal Excitation. After the specimens are preliminarily checked by the free vibration test, ERIS is subjected to sinusoidal excitation for further experimental

examination. For a nonlinear system, the dynamic behavior is not only affected by the frequency but also by the amplitude of excitation; thus, the effect of the amplitude of excitation should be considered. However, due to the mechanical limitations of the shaking table, the performance of ERIS subjected to excitation with a large amplitude could not be carried out. Thus, such evaluation was conducted by numerical simulation and compared with the experimental

TABLE 4: Test items for seismic excitation.

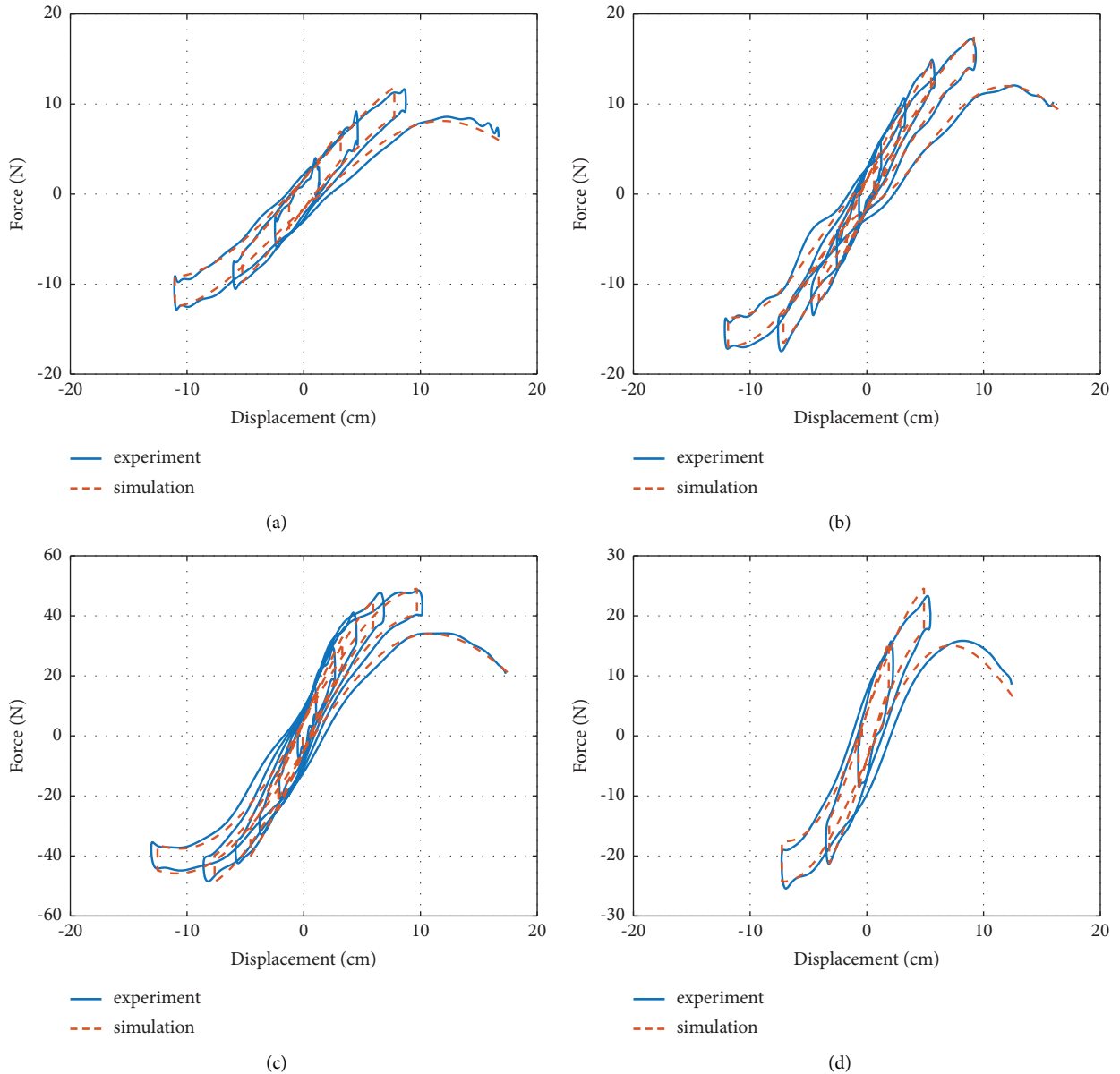|	SP1	SP2	SP3	SP4
		PGD (cm)		
Imperial Valley-06	7.5	7.5	7.5	7.5
	6.0	6.0	6.5	6.5
	4.0	4.0	4.5	5.0
Chi-Chi	6.0	6.0	7.0	7.0
	5.0	5.0	6.0	5.0
	4.0	4.0	5.0	4.0

(a)

(b)

(c)

(d)

FIGURE 9: Hysteresis loops under free vibration: (a) SP1, (b) SP2, (c) SP3, and (d) SP4.

results. The two performance indices, the acceleration ratio and displacement ratio, versus the PGAs of SP1 are illustrated in Figure 10. In Figure 10(a), the acceleration ratio is equal to one regardless of the frequency when the amplitude is small. This could be explained by reference to Figure 10(b), in which the displacement ratio is zero in the corresponding amplitude range. This means that the system is not active. In other words, the shear force of the system has not yet overcome the friction force. For the case of frequency equal to $2f_0$, the acceleration ratio is generally smaller than one,
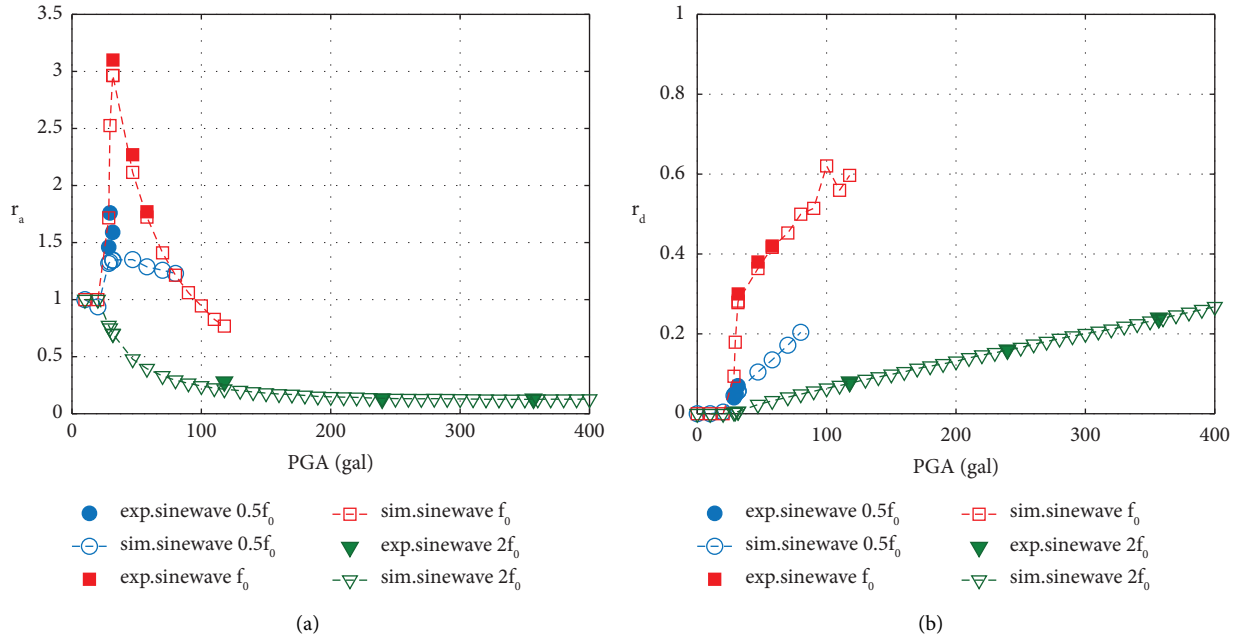
FIGURE 10: Performance of SP1 under sinusoidal excitation: (a) acceleration ratio vs. PGA and (b) displacement ratio vs. PGA.

which implies that ERIS is effective, and the acceleration ratio decreases with an increase in amplitude. For the other two frequency cases $0.5f_0$ and f_0, the acceleration and displacement ratios are much higher than in the case of $2f_0$ under the same amplitude. Moreover, for an isolation system subjected to a sinusoidal excitation with a frequency equal to or lower than the isolation frequency, excessive isolation displacement can be observed. Therefore, the applicable range of amplitude for both the $0.5f_0$ and f_0 cases is much smaller than for the $2f_0$ case. For each case, the experimental results labeled by solid marker are close to the simulation results labeled by the dashed line. In other words, the mathematical model using the identified friction coefficient can accurately represent the behavior of ERIS.

Similarly, Figure 11 illustrates the relationship between the performance index and the amplitude of sinusoidal excitation for SP2. Similar results are observed when the amplitude is smaller than approximately 120 gal. In other words, the case of the excitation frequency equal to f_0 generally has the highest acceleration and displacement responses, the case of $2f_0$ has the lowest responses, and the performance of the $0.5f_0$ case lies between the other two. If the frequency of excitation is double the linearized frequency (i.e., $f_{ext} = 2f_0$), ERIS performs reasonably well at reducing the acceleration without large displacement responses in the considered amplitude range. The comparison between the experimental and simulation results in this figure also indicates that the simulation results are pretty close to the experimental results for all three frequency cases (comparison between the dashed lines and solid markers). The performances of SP3 and SP4 subjected to sinusoidal excitation are shown in Figures 12 and 13, and similar results are observed. Both specimens perform reasonably well under sinusoidal excitation with a frequency higher than the linearized frequency of the system.

The acceleration ratios for the considered range of amplitude are small, and the maximum displacement ratios are not over 0.2 for the two specimens when the amplitude equals 800 gal (i.e., for SP3 and SP4). When the frequency of excitation is changed to the linearized frequency or half this value, they are both ineffective at acceleration reduction and the applicable ranges of amplitude for the two specimens are also narrow due to the excessive displacement. Nevertheless, the simulation results for the two specimens approximate the experimental results.

3.3.3. Seismic Excitation. In addition to being subjected to sinusoidal excitation, the system is subjected to seismic excitation to investigate more realistic practical applications. Numerical simulation results are also provided to extensively demonstrate the performance of certain cases that could not be examined by shaking table tests or by comparison with the experimental results. Two seismic excitations, the Imperial Valley (station Coachella Canal #4) and Chi-Chi (station TCU102), are adopted for various amplitudes of excitation (Table 4). Additionally, a linear system with an isolation period of two seconds and a friction coefficient of 2% is also simulated to give a baseline for discussion. The comparison of four specimens and the linear system subjected to the two ground motions above are, respectively, illustrated in Figures 14 and 15. The results of different cases are categorized by different colors (e.g., the linear system is colored green, and SP4 is colored purple). The simulation and experimental results for each specimen are represented by a solid line and a dot. The experimental results of four ERIS specimens, subjected to the two ground motions, are compared with the simulation results of the linear system and tabulated in Tables 5 and 6, respectively.
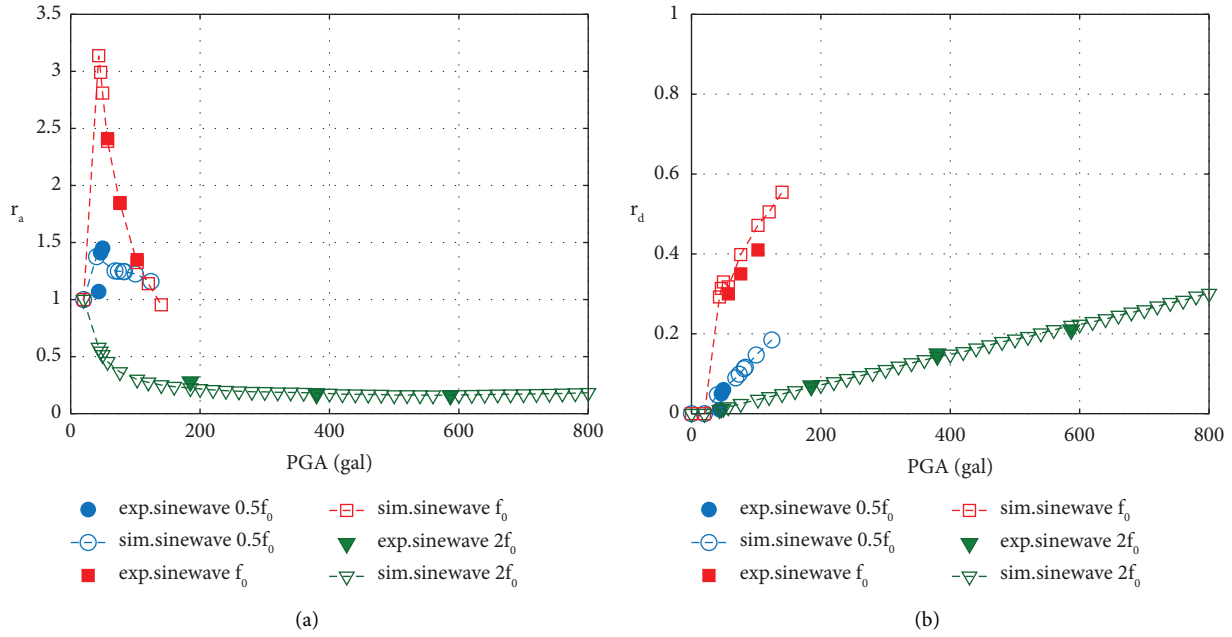
FIGURE 11: Performance of SP2 under sinusoidal excitation: (a) acceleration ratio vs. PGA and (b) displacement ratio vs. PGA.
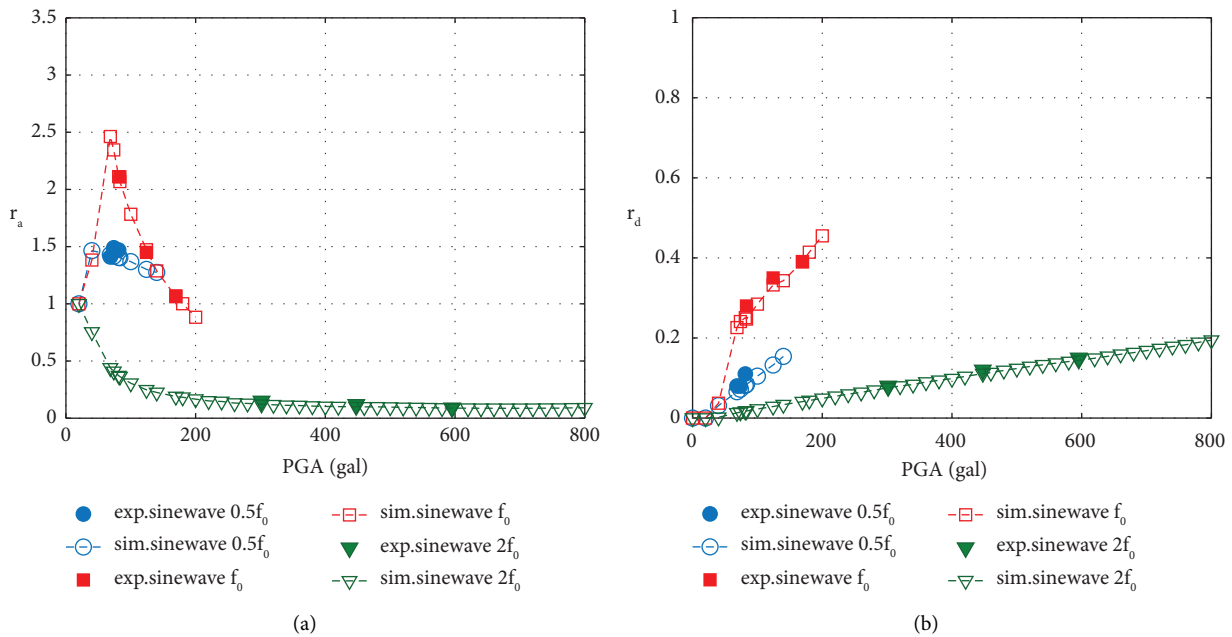

FIGURE 12: Performance of SP3 under sinusoidal excitation: (a) acceleration ratio vs. PGA and (b) displacement ratio vs. PGA.

(1) Far-Field Imperial Valley Earthquake Motion. For the seismic performances under the far-field Imperial Valley earthquake motion, it is clear that all the ERIS cases and the linear system are effective in mitigating the acceleration response with different degrees except for some low PGA cases (Figure 14(a)). The systems are not activated for those low PGA cases due to excessive inherent frictional damping. Generally, the larger the PGA amplitude, the better the acceleration reduction. SP1 has the lowest acceleration ratio, followed by the linear system, SP2, SP3, and SP4 in that order. This performance order of the acceleration ratio for the four ERIS specimens follows the order of the linearized frequency (i.e., from low to high, Table 1). The performance in acceleration for SP1 and the linear system are quite close. Both SP1 and the linear system have about 60% acceleration reduction when the PGA is higher than 100 gal. However, it shows a big difference when comparing the isolation displacement between the SP1 and the linear system. SP1 has lower isolation displacement than the linear system (Figure 14(b), blue line and green line). For all the cases (i.e.,
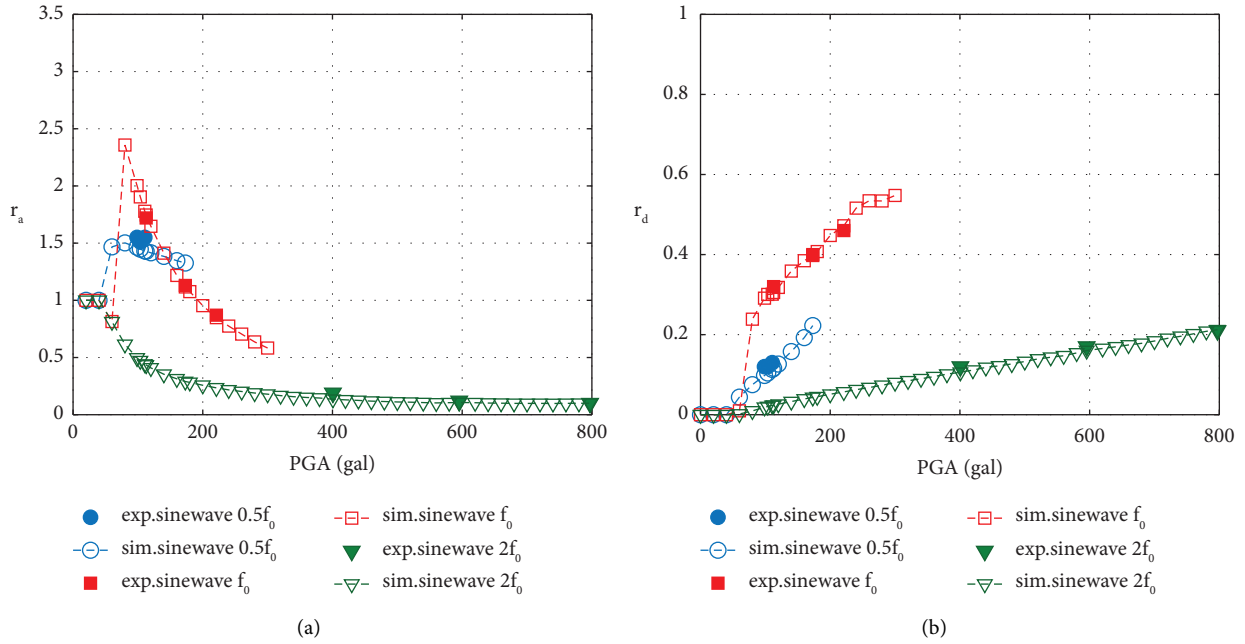
FIGURE 13: Performance of SP4 under sinusoidal excitation: (a) acceleration ratio vs. PGA and (b) displacement ratio vs. PGA.
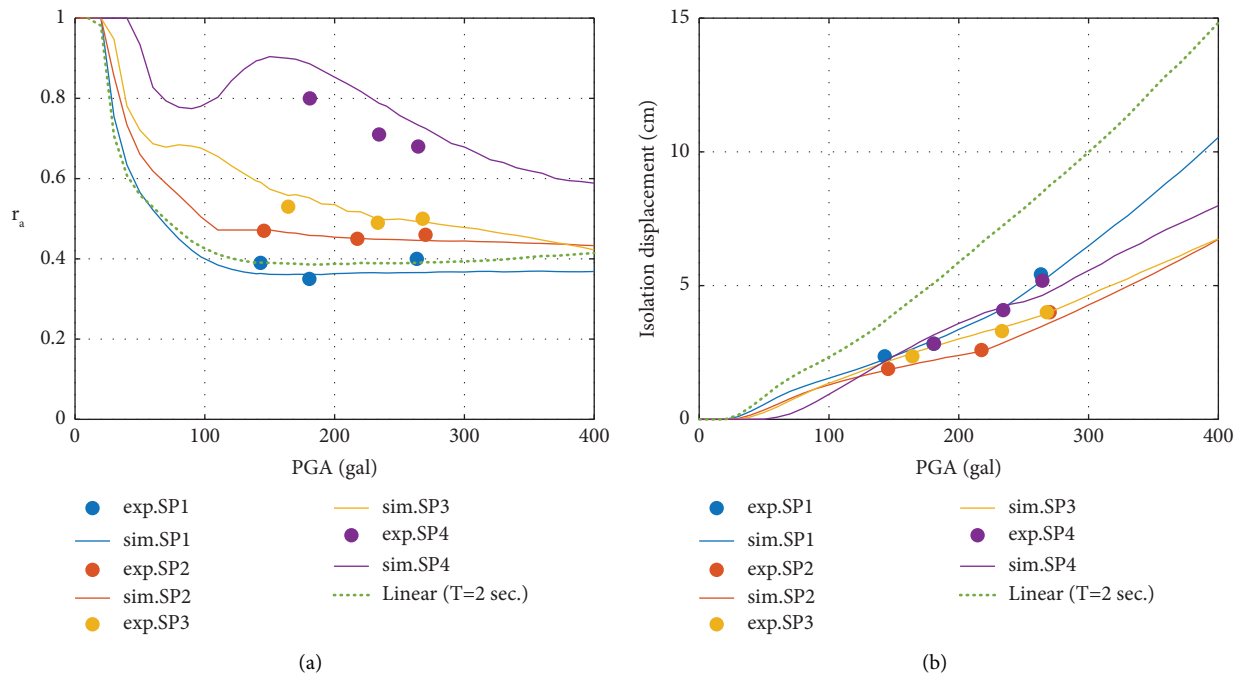

FIGURE 14: Seismic performance of ERIS compared with the linear system ($T = 2 \sec, \mu = 0.02$) under the Imperial Valley earthquake motion: (a) acceleration ratio vs. PGA and (b) displacement vs. PGA.

four ERIS specimens and the linear system), the isolation displacement increases with the increase of PGA, the linear system has higher isolation displacement than the other four ERIS specimens. In general, the significant difference in the acceleration ratio for the four ERIS specimens is not observed in isolation displacement, but obviously, SP1 still requires higher isolation displacement than the other three

ERIS specimens to obtain good acceleration reduction. Moreover, the experimental results for the two indices tabulated in Table 5 clearly show that the ERIS performs well at acceleration reduction under the Imperial Valley earthquake motion for various degrees of isolation displacement. Additionally, the vertical acceleration ratios are all smaller than one, which means that the ERIS can achieve good
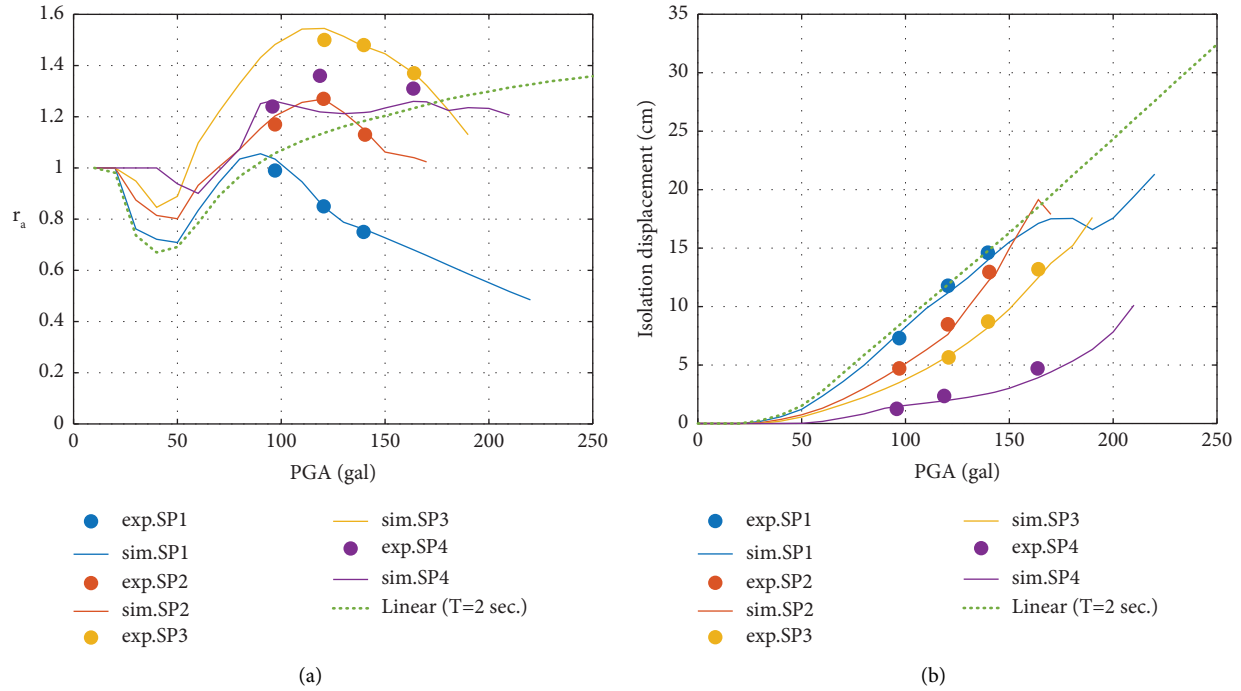
(a)

(b)

FIGURE 15: Seismic performance of ERIS compared with the linear system ($T = 2$ sec, $\mu = 0.02$) under the Chi-Chi earthquake motion: (a) acceleration ratio vs. PGA and (b) displacement vs. PGA.

TABLE 5: Test results of ERIS specimens and simulation results of the linear system under far-field Imperial Valley earthquake.

Specimen	PGD (cm)*	PGA (gal)§	r_d	Max. disp. (cm)	r_a	$r_{a,v}$
SP1	7.5	263.3	0.23	5.42	0.40	0.15
	6.0	180.5	0.12	2.83	0.35	0.11
	4.0	142.9	0.10	2.36	0.39	0.08
SP2	7.5	270.0	0.17	4.01	0.46	0.19
	6.0	217.5	0.11	2.59	0.45	0.16
	4.0	145.5	0.08	1.88	0.47	0.11
SP3	7.5	267.9	0.17	4.01	0.50	0.35
	6.5	233.3	0.14	3.30	0.49	0.32
	4.5	164.2	0.10	2.36	0.53	0.28
SP4	7.5	264.4	0.33	5.18	0.68	0.76
	6.5	234.3	0.26	4.08	0.71	0.67
	5.0	180.9	0.18	2.83	0.80	0.43
Linear† (T = 2 s.)	—	270.0	—	8.74	0.39	—
	—	230.0	—	7.09	0.39	—
	—	180.0	—	5.08	0.39	—
	—	160.0	—	4.47	0.39	—
	—	140.0	—	3.54	0.39	—

*Displacement amplitude for command. §Actual measurement of acceleration for each test for four specimens. †Results for the linear system are obtained from numerical simulation.

TABLE 6: Test results of ERIS specimens and simulation results of the linear system under near-fault Chi-Chi earthquake.

Specimen	PGD (cm)*	PGA (gal)§	r_d	Max. disp. (cm)	r_a	$r_{a,v}$
SP1	6.0	139.7	0.62	14.61	0.75	0.60
	5.0	120.4	0.50	11.78	0.85	0.53
	4.0	97.0	0.31	7.30	0.99	0.36
SP2	6.0	140.3	0.55	12.96	1.13	1.38
	5.0	120.4	0.36	8.48	1.27	0.98
	4.0	97.0	0.20	4.71	1.17	0.50
SP3	7.0	164.0	0.56	13.19	1.37	1.51
	6.0	139.7	0.37	8.72	1.48	1.05
	5.0	120.8	0.24	5.65	1.50	0.67
SP4	7.0	163.6	0.30	4.71	1.31	0.53
	5.0	118.6	0.15	2.36	1.36	0.28
	4.0	95.8	0.08	1.26	1.24	0.14
Linear† (T = 2 s)	—	160.0	—	18.51	1.23	—
	—	140.0	—	14.75	1.18	—
	—	120.0	—	11.88	1.14	—
	—	90.0	—	7.34	1.02	—

*Displacement amplitude for command. §Actual measurement of acceleration for each test for four specimens. †Results for the linear system are obtained from numerical simulation.

control performance in the horizontal direction without sacrificing too much vertical acceleration. Conclusively, for the ERIS subjected to far-field Imperial Valley earthquake motion, it is effective in mitigating horizontal acceleration without too much isolation displacement and vertical acceleration to trade-off, and it potentially performs even

better than the linear system in both acceleration and displacement (e.g., SP1 in Figure 14).

(2) Near-Fault Chi-Chi Earthquake Motion. After comparing and discussing the control performance for the four ERIS specimens and the linear system subjected to Imperial Valley earthquake motion, the control performances of the four
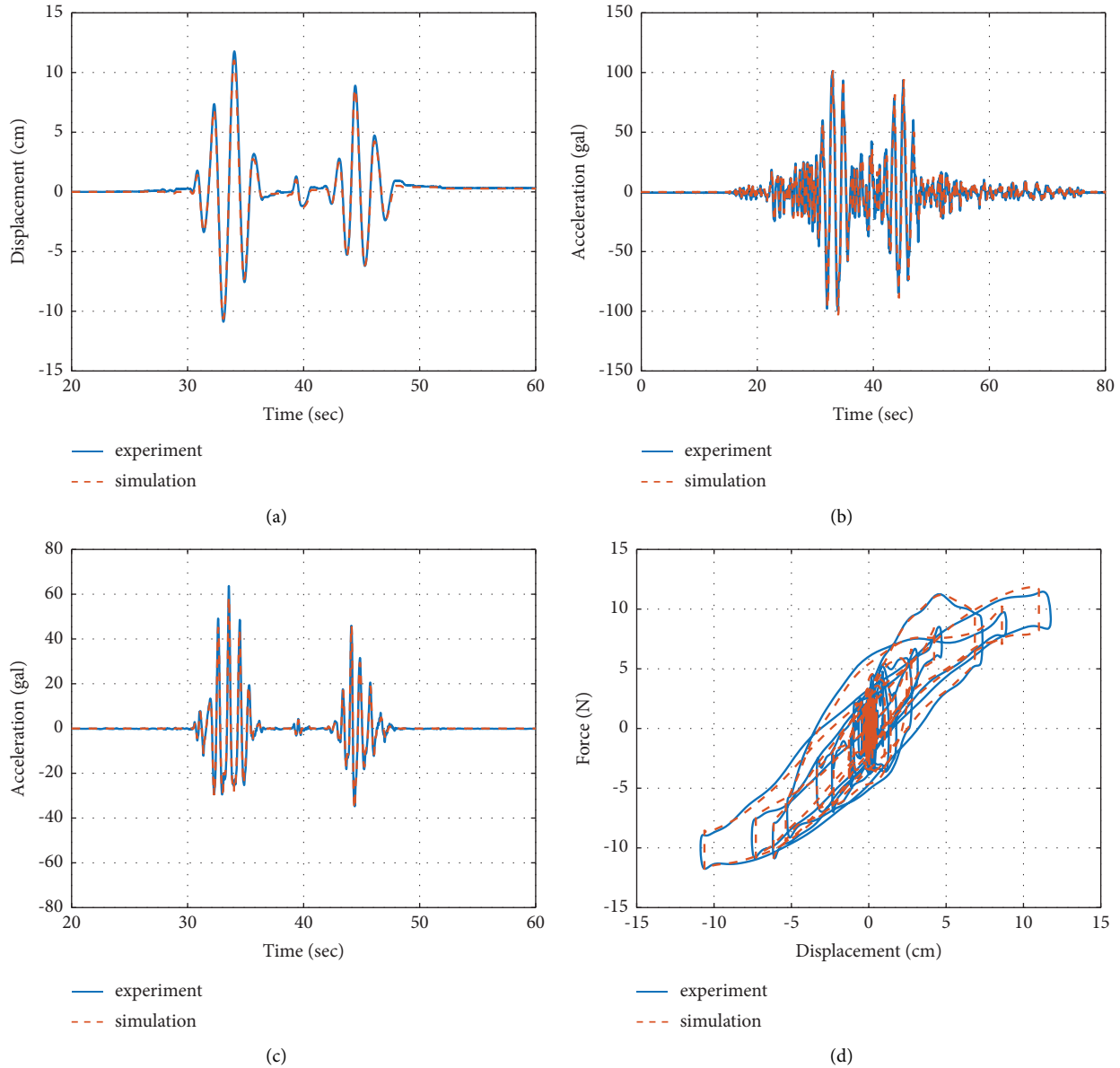
(a)

(b)

(c)

(d)

FIGURE 16: Time history and hysteretic comparison of SP1 under the Chi-Chi earthquake motion with a PGD of 50 mm: (a) displacement, (b) horizontal acceleration, (c) vertical acceleration, and (d) hysteresis.

specimens and the linear system subjected to the Chi-Chi earthquake ground motion are further investigated and compared (Figure 15). From Figure 15(a), it is evident that the five isolation cases (i.e., four ERIS and the linear system) are no longer so effective when they are excited by the near-fault Chi-Chi earthquake motion, and the applicable range of amplitude for the four ERIS specimens is narrower than that of the far-field Imperial Valley earthquake motion case. Based on the acceleration ratios shown in Figure 15(a), the linear system is considered only to be effective to various degrees when the amplitude of excitation is lower than approximately 80 gal, although it increases as the amplitude increases (green line). In general, SP3 has the highest accelerations (yellow line), followed by SP4 and SP2 in that order (purple and red lines, respectively). These three

specimens could not exhibit the desired control performance under the Chi-Chi earthquake motion for the considered amplitudes, and this outcome could be observed from the experimental results shown in Table 6 (i.e. large acceleration ratios). However, differing from the other specimens, SP1 shows better performance, as does the linear system, especially when the amplitude of excitation continues to increase (blue line). The isolation displacements for the four specimens and the linear system are illustrated in Figure 15(b). In general, the linear system has the highest isolation displacement compared with the four specimens, and it increases with an increase in amplitude. For the four specimens, SP1 requires the highest isolation displacement to achieve a better acceleration reduction, followed by SP2, SP3, and SP4 in that order.

TABLE 7: Comparison of experimental and simulation results of SP1 subjected to the Chi-Chi earthquake motion (PGD: 50 mm).

Specimen	Case	Disp. ratio (r_d)	Acc. ratio (r_a)	Residual disp. (cm)
	Experiment	0.50	0.845	0.32
SP1 μ_d: 0.018	Simulation	0.47	0.853	0.28
	Error (%)	6.0	0.95	12.5

It should be noted that specimens SP2, SP3, and SP4 have higher acceleration ratios and lower displacements than the linear one until the excitation amplitude is higher than some level. This is because the linearized frequencies of specimens SP2 to 4 are close to 1 Hz (1 second) which is higher than the dominant frequency of Chi-Chi earthquake motion (Table 1 and Figure 8(d)). As the PGA increases, the displacement of specimens SP2 to 4 also increases, resulting in a lower vibration frequency to reduce acceleration response. This feature of ERIS could be reviewed in the section of the parametric study (Figure 4). On the other hand, the linearized frequency is equal to 0.628 Hz of SP1, which is initially lower than the other three specimens, and the vibration frequency decreases with the increase of PGA. Once the frequency of isolation systems is lower than the frequency of excitation, a larger displacement and lower acceleration could be expected, this is what could be observed in the SP1 case in Figure 15. According to the comparison between the linear system and the four specimens, it can be seen that ERIS indeed has the potential to perform better than a conventional isolation system; however, the key parameters that play an important role in control performance need to be designed carefully to obtain a better performance in either acceleration reduction or isolation displacement.

3.3.4. Mathematical Model Verification. By comparing the simulation and experimental results for the four specimens in Figures 14 and 15, it is evident that the two results generally agree with each other under both considered earthquake motions. However, as mentioned previously, the circular roller with a radius of 5 cm is adopted in SP4 to replace the roller with a radius of 7.5 cm used in the SP1, SP2, and SP3 specimens. This change results in a larger deviation of the friction coefficient and causes a larger error between the simulation and experimental results of SP4 (Figures 14 and 15, line and dot colored in purple). To demonstrate the seismic response of ERIS in detail, the time histories and hysteresis of SP1 subjected to the Chi-Chi earthquake motion with PGD equal to 50 mm are taken as an example and illustrated in Figure 16. The blue solid line and red dashed line represent the experimental and simulation results, respectively. It is evident that the simulation results are reasonably close to the experimental results for both the acceleration and displacement response. The comparison of peak values is tabulated in Table 7. The simulation errors relative to the experimental results for the displacement and acceleration ratios are 6.0% and 0.95%, respectively. Moreover, the restoring capability of ERIS is strong, as indicated by the small residual displacements for the simulation and experimental results, 0.28 mm and 0.32 mm, respectively.

4. Conclusions

The concept of the eccentric rolling isolation system proposed in previous research was experimentally verified with a prototype of a unilateral mechanism consisting of one payload platform, four spur gears (as rollers), and two racks. The mathematical model was also modified by further considering the inertia of the roller, which can significantly affect the dynamic behavior when ERIS is implemented for equipment isolation. The seismic performance and feasibility of ERIS were carefully examined by numerical simulations and shaking table tests. The key parameters that determine the behavior of ERIS were investigated by numerical simulation of free vibration and forced vibration with sinusoidal and seismic excitations. The mathematical model was further confirmed by comparing the simulation results with the experimental results. Consequently, the feasibility of the proposed ERIS mechanism and the validity of the mathematical model were both verified. Some concluding remarks are summarized as follows:

(1) Based on the sensitivity study of the mass ratio, the simulation results revealed that the inertia of the rollers does affect the dynamic behavior of ERIS. A larger mass results in a larger mass ratio and lower isolation frequency, which is desired in seismic isolation. Additionally, by introducing the inertia of the circular rollers, the linearized frequency of ERIS remains low without adopting a big circular roller (i.e., a large radius), which helps downsize the ERIS mechanism and makes its design more flexible.

(2) The mathematical model modified with the consideration of the inertia of the roller was derived and successfully verified by shaking table tests. The roles of the key design parameters including the radius of the roller, mass ratio, and eccentricity could be captured and reproduced by the model.

(3) For the proposed ERIS mechanism, the assumption of effective friction damping with Coulomb's model to represent the energy dissipation of ERIS was also verified. For such a rolling mechanism, the inherent friction may be induced by many movable components; however, it can be simplified and represented by one effective friction coefficient for the entire proposed ERIS mechanism.

(4) ERIS performs well when the system is subjected to far-field earthquake motions. Relative to the considered linear system, the ERIS has similar or a little bit better acceleration reduction with a smaller demand of isolation displacement.

(5) When near-fault ground motions are considered, generally, the seismic performance of ERIS subjected to near-fault ground motions is not as good as the performance under far-field earthquake motions. However, ERIS can also potentially mitigate the acceleration response if appropriately designed. Relative to the considered linear system, a sound acceleration reduction could be performed by ERIS with a similar demand of isolation displacement.

(6) Based on the numerical and simulation results, the behavior of the nonlinear ERIS system is sensitive to various design parameters and excitations; thus, they should be carefully considered in practical applications.

(7) The feasibility of the prototype ERIS is preliminarily verified, and the specification designed as specimen SP1 generally shows better performances under the considered excitations, which exhibits a good design reference for practical implementations.

(8) The bilateral mechanism, design procedure, and structural isolation of the ERIS are the future scopes.

Data Availability

The data used to support the findings of this study are available from the corresponding author upon request.

Conflicts of Interest

The authors declare that they have no conflicts of interest.

Acknowledgments

References

[1] N. Makris, "Seismic isolation: early history," *Earthquake Engineering and Structural Dynamics*, vol. 48, no. 2, pp. 269–283, 2018.

[2] N. Nabid, I. Hajirasouliha, and M. Petkovski, "Simplified method for optimal design of friction damper slip loads by considering near-field and far-field ground motions," *Journal of Earthquake Engineering*, vol. 25, no. 9, pp. 1851–1875, 2019.

[3] G. P. Warn and K. L. Ryan, "A review of seismic isolation for buildings: historical development and research needs," *Buildings*, vol. 2, no. 3, pp. 300–325, 2012.

[4] A. Martelli and M. Forni, "Seismic isolation and other antiseismic systems: recent applications in Italy and worldwide," *Seismic Isolation and Protective Systems*, vol. 1, no. 1, pp. 75–123, 2010.

[5] A. Martelli, M. Forni, and P. Clemente, "Recent worldwide application of seismic isolation and energy dissipation and conditions for their correct use," in *Proceedings of 15th World Conference on Earthquake Engineering (15WCEE)*, Lisbon, Portugal, September 2012.

[6] Y. Nakamura and K. Okada, "Review on seismic isolation and response control methods of buildings in Japan," *Geo-environmental Disasters*, vol. 6, no. 1, p. 7, 2019.

[7] N. Kani and S. Katsuta, "Seismic isolation retrofit for existing buildings in Japan," in *Proceedings of ATC & SEI 2009 Conference on Improving the Seismic Performance of Existing Buildings and Other Structures*, San Francisco, CA, USA, December 2009.

[8] P. S. Harvey and K. C. Kelly, "A review of rolling-type seismic isolation: historical development and future directions," *Engineering Structures*, vol. 125, pp. 521–531, 2016.

[9] C.-Y. Yang, S.-J. Wang, C.-K. Lin, L.-L. Chung, and M.-C. Liou, "Analytical and experimental study on sloped sliding-type bearings," *Structural Control and Health Monitoring*, vol. 28, no. 11, 2021.

[10] S.-J. Wang, J.-S. Hwang, K.-C. Chang et al., "Sloped multi-roller isolation devices for seismic protection of equipment and facilities," *Earthquake Engineering and Structural Dynamics*, vol. 43, no. 10, pp. 1443–1461, 2014.

[11] R. S. Jangid and J. M. Kelly, "Base isolation for near-fault motions," *Earthquake Engineering and Structural Dynamics*, vol. 30, no. 5, pp. 691–707, 2001.

[12] J. Shen, M.-H. Tsai, K.-C. Chang, and G. C. Lee, "Performance of a seismically isolated bridge under near-fault earthquake ground motions," *Journal of Structural Engineering*, vol. 130, no. 6, pp. 861–868, 2004.

[13] H. Anajafi, K. Poursadr, M. Roohi, and E. Santini-Bell, "Effectiveness of seismic isolation for long-period structures subject to far-field and near-field excitations," *Frontiers in Built Environment*, vol. 6, 2020.

[14] F. Mazza and R. Labernarda, "Effects of near-fault acceleration and non-acceleration pulses on pounding between in-plan irregular fixed-base and base-isolated buildings," *Structural Control and Health Monitoring*, vol. 29, no. 9, 2022.

[15] American Society of Civil Engineers, *Minimum Design Loads for Buildings and Other Structures, Asce/SEI 7-05,-10,-16*, ASCE, Reston, VA, USA, 2005.

[16] R. S. Jangid, "Optimum lead–rubber isolation bearings for near-fault motions," *Engineering Structures*, vol. 29, no. 10, pp. 2503–2513, 2007.

[17] R. S. Jangid, "Optimum friction pendulum system for near-fault motions," *Engineering Structures*, vol. 27, no. 3, pp. 349–359, 2005.

[18] M. Bhandari, S. D. Bharti, M. K. Shrimali, and T. K. Datta, "The numerical study of base-isolated buildings under near-field and far-field earthquakes," *Journal of Earthquake Engineering*, vol. 22, no. 6, pp. 989–1007, 2017.

[19] C. P. Providakis, "Effect of supplemental damping on LRB and FPS seismic isolators under near-fault ground motions," *Soil Dynamics and Earthquake Engineering*, vol. 29, no. 1, pp. 80–90, 2009.

[20] W. Liu and K. Ikago, "Causal implementation of rate-independent linear damping for the seismic protection of low-frequency structures," *Structures*, vol. 35, pp. 274–288, 2022.

[21] W. Liu and K. Ikago, "Performance of a passive rate-independent damping device in a seismically isolated multistory building," *Structural Control and Health Monitoring*, vol. 29, no. 6, Article ID e2941, 2022.

[22] W. Liu and J. Liu, "Experimental realization of rate-independent linear damping using a semiactive damper to enhance the seismic performance of low-frequency structures," *Journal of Building Engineering*, vol. 70, Article ID 106374, 2023.

[23] W. Liu and K. Ikago, "Experimental study of earthquake input energy of low-frequency structures equipped with a passive rate-independent damping device," *Structural Control and Health Monitoring*, vol. 29, no. 2, Article ID e2883, 2022.

[24] W. Liu and K. Ikago, "Feasibility of physical implementation of rate-independent linear damping to protect multistory low-frequency structures," *Journal of Sound and Vibration*, vol. 528, Article ID 116893, 2022.

[25] W. Liu, K. Ikago, Z. Wu, and I. Fukuda, "Modified tuned Maxwell–Wiechert model for improving seismic performance of base-isolated structures," *Journal of Building Engineering*, vol. 54, Article ID 104616, 2022.

[26] W. Liu, Y.-Q. Ni, K. Ikago, and W. K. Ao, "Seismic control of base-isolated structures using rate-independent damping devices," *Journal of Building Engineering*, vol. 78, Article ID 107744, 2023.

[27] Y.-P. Zhu, Z. Q. Lang, K. Fujita, and I. Takewaki, "Analysis and design of nonlinear seismic isolation systems for building structures—an overview," *Frontiers in Built Environment*, vol. 8, 2023.

[28] R. A. Ibrahim, "Recent advances in nonlinear passive vibration isolators," *Journal of Sound and Vibration*, vol. 314, no. 3-5, pp. 371–452, 2008.

[29] P. S. Balaji and K. Karthik SelvaKumar, "Applications of nonlinearity in passive vibration control: a review," *Journal of Vibration Engineering & Technologies*, vol. 9, no. 2, pp. 183–213, 2021.

[30] L.-Y. Lu, T.-Y. Lee, and S.-W. Yeh, "Theory and experimental study for sliding isolators with variable curvature," *Earthquake Engineering and Structural Dynamics*, vol. 40, no. 14, pp. 1609–1627, 2011.

[31] L.-Y. Lu, T.-Y. Lee, S.-Y. Juang, and S.-W. Yeh, "Polynomial friction pendulum isolators (PFPIs) for building floor isolation: an experimental and theoretical study," *Engineering Structures*, vol. 56, pp. 970–982, 2013.

[32] L.-Y. Lu, H.-W. Huang, Y. Wu, and S.-J. Wang, "Theory and experimental verification of a double sliding isolator with variable curvature," *Engineering Structures*, vol. 238, Article ID 112265, 2021.

[33] S. Nepal and M. Saitoh, "Improving the performance of conventional base isolation systems by an external variable negative stiffness device under near-fault and long-period ground motions," *Earthquake Engineering and Engineering Vibration*, vol. 19, no. 4, pp. 985–1003, 2020.

[34] I. Kovacic, M. J. Brennan, and T. P. Waters, "A study of a nonlinear vibration isolator with a quasi-zero stiffness characteristic," *Journal of Sound and Vibration*, vol. 315, no. 3, pp. 700–711, 2008.

[35] K. Ye, J. C. Ji, and T. Brown, "Design of a quasi-zero stiffness isolation system for supporting different loads," *Journal of Sound and Vibration*, vol. 471, Article ID 115198, 2020.

[36] D. Liu, Y. Liu, D. Sheng, and W. Liao, "Seismic response analysis of an isolated structure with QZS under near-fault vertical earthquakes," *Shock and Vibration*, vol. 2018, Article ID 9149721, 12 pages, 2018.

[37] L. L. Chung, C. Y. Yang, H. M. Chen, and L. Y. Lu, "Dynamic behavior of nonlinear rolling isolation system," *Structural Control and Health Monitoring*, vol. 16, no. 1, pp. 32–54, 2009.

[38] C.-Y. Yang, C.-H. Hsieh, L.-L. Chung, H.-M. Chen, and L.-Y. Wu, "Effectiveness of an eccentric rolling isolation system with friction damping," *Journal of Vibration and Control*, vol. 18, no. 14, pp. 2149–2163, 2011.

[39] The MathWorks Inc, *Matlab, 9.7.0.1190202 (R2019b)*, The MathWorks Inc, Natick, MA, USA, 2018.

[40] R. W. Clough and J. Penzien, *Dynamics of Structures*, McGraw-Hill, New York, NY, USA, 2nd edition, 1993.

[41] Khk Co Ltd, "KHK-USA," 2023, https://www.khkgears.us/.

[42] M. Davoodi, M. Sadjadi, P. Goljahani, and M. Kamalian, "Effects of near-field and far-field earthquakes on seismic response of SDOF system considering soil-structure interaction," in *Proceedings of 15th World Conference on Earthquake Engineering (15WCEE)*, Lisbon, Portugal, September 2012.